

Plasmon resonance based gold nanoparticle doped optical fibre strain sensing

Wang, Xiang; Benedictus, Rinze; Groves, Roger M.

DOI

[10.1016/j.optlastec.2022.108272](https://doi.org/10.1016/j.optlastec.2022.108272)

Publication date

2022

Document Version

Final published version

Published in

Optics and Laser Technology

Citation (APA)

Wang, X., Benedictus, R., & Groves, R. M. (2022). Plasmon resonance based gold nanoparticle doped optical fibre strain sensing. *Optics and Laser Technology*, 153, Article 108272. <https://doi.org/10.1016/j.optlastec.2022.108272>

Important note

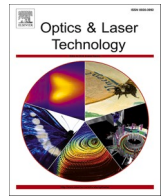
To cite this publication, please use the final published version (if applicable). Please check the document version above.

Copyright

Other than for strictly personal use, it is not permitted to download, forward or distribute the text or part of it, without the consent of the author(s) and/or copyright holder(s), unless the work is under an open content license such as Creative Commons.

Takedown policy

Please contact us and provide details if you believe this document breaches copyrights. We will remove access to the work immediately and investigate your claim.



Full length article

Plasmon resonance based gold nanoparticle doped optical fibre strain sensing

Xiang Wang^{*}, Rinze Benedictus, Roger M. Groves

Faculty of Aerospace Engineering, Delft University of Technology, Delft 2629 HS, the Netherlands

ARTICLE INFO

Keywords:

Gold nanoparticle
Optical fibre
Plasmon resonance
Strain sensing

ABSTRACT

Strain-based structural health monitoring (SHM) relies on high performance strain sensing methods. Gold nanoparticle (NP) doped fibre optic sensors not only have the potential to increase the intensity of the backscattered signal to increase the signal to noise ratio but also have plasmon resonance peaks in the visible light range. The spectral peak shift of the plasmon resonance may be used for strain sensing. In this paper, the spectral peak shift of the plasmon resonance of an optical fibre containing gold NPs under axial strain was analysed. A modified Lorentz-Drude (LD) model with the T-matrix method was used and the spectral peak shifts of spheroidal NPs under strain were calculated. An approximate analytical expression was derived for faster calculation. The modelling presented in this paper shows that the ratio of the change of the peak wavelength to the strain can be related to the refractive index (RI) change of the optical fibre under strain, the shape change of the gold NP, and the RI change of the gold NP. The peak shift was also observed experimentally in an optical adhesive containing gold NPs under compression. The peak shifts were analysed at different RI of the optical fibres, 1.35, 1.45, 1.55 and 1.65 respectively, in order to cover the range of RI of fused silica and some polymer materials. The results confirm experimentally that the applied axial strain can induce the peak wavelength shift by the NPs. By choosing a different optical fibre or the properties of the NPs, the wavelength change ratio has the potential to be tuned, which may be used for highly sensitive strain sensing.

1. Introduction

Structural health monitoring (SHM) can support the maintenance of the of engineering structures for a long life in service in aerospace [1] and civil engineering [2]. Sensors are used to perform measurements for diagnoses or for prediction of damage or failure [3] in the structure in order to prevent accidents caused by structural damage or failure. One type of SHM is strain-based SHM [4]. By obtaining strain information from the structure under loading using sensors along with the algorithms to process the data, the structural integrity of the structure can be evaluated. There are many types of strain sensors for SHM [5]. For example, resistance strain gages [6], Fabry-Pérot cavity based optical strain gages [7], fibre Bragg grating based optical strain gages [8–10] and distributed fibre optic based strain gages [11]. Compared with traditional resistance strain gages, fibre optic sensors have the advantage of being able to be embedded into the structure, for example composites, and are light weight, and have a small size, high sensitivity and immunity to electromagnetic interference [12], etc. Due to these advantages, fibre optic sensors have been widely used for the monitoring

of the structures in aerospace [13,14] and in civil engineering [15,16].

In recent years, nanoparticle (NP) doped optical fibre sensing has attracted the interest of researchers [17–20] because the doped NPs in the core of the optical fibre enhance the backscattered light dramatically. The enhanced backscattered signal is beneficial to the signal to noise ratio for strain detection. Gold is one of the potential materials for NP doped fibre optic sensing due to its high backscattering properties [21]. Gold NPs not only increase the intensity of backscattered light but also have a high extinction for light transmission, which is caused by localized surface plasmon resonance (LSPR) [22]. Surface plasmon resonance (SPR) a phenomenon caused by the resonance of free electrons in a metal due to an incident light wave. Gold as a metal can be used as the material for SPR. There are several applications for optical fibre sensors based on the SPR of gold. For example, coating a thin gold layer on optical fibres to achieve twist detection [23,24] or to achieve high sensitive flow rate detection [25] or to achieve refractive index (RI) detection [26]. Gold NPs as a metallic NPs has small geometric size compared with the wavelengths of visible light in all spatial dimensions. Therefore, the SPR for gold NPs is localized. The SPR based sensors may

^{*} Corresponding author.

E-mail addresses: xiang.wang@tudelft.nl (X. Wang), r.benedictus@tudelft.nl (R. Benedictus), r.m.groves@tudelft.nl (R.M. Groves).

<https://doi.org/10.1016/j.optlastec.2022.108272>

Received 22 February 2022; Received in revised form 14 April 2022; Accepted 3 May 2022

Available online 11 May 2022

0030-3992/© 2022 The Author(s). Published by Elsevier Ltd. This is an open access article under the CC BY license (<http://creativecommons.org/licenses/by/4.0/>).

have advantages in some applications for example higher RI sensitivity compared with LSPR based sensors [27]. However, the sensitivity based on LSPR is tunable based on the shape of the NPs. In this circumstance, tunable sensitivity strain sensing may be achieved via detecting transmitted light in the visible light range (generally the plasmon resonance peak is in the visible light range for small size spherical gold NPs[28]) with an optical fibre containing gold NPs in the core. The wavelength range can be different from that used for distributed fibre optic sensing strain detection, for example the light wavelengths for LUNA ODISI-B is around 1550 nm in near Infrared wavelength range. Previous research has shown that the RI of the gold NP will change under strain change [29–31]. Along with the shape change of the NPs and the RI change of the optical fibre, the resonance peak may shift. Therefore, doping gold NP into the core of the optical fibre may have the potential for the strain detection based on the plasmon resonance peak shift in the visible light range. Therefore, it may be an auxiliary strain detection method along with distributed fibre optic sensing based on Rayleigh scattering in different wavelength ranges. However, the behaviour of the peak wavelength change under strain change along optical fibre has not yet been fully studied.

In this work, the strain sensing feasibility of gold NP doped optical fibre will be investigated using analytical expressions, simulations and experiments. First the modified Lorentz-Drude model is proposed to show the RI change of spherical gold NP under strain change. Then, based on the modified Lorentz-Drude (LD) model and the T-matrix method (also called the extended boundary-condition method (EBCM) method) [32,33] for light scattering by spheroidal NP, the plasmon resonance peak shift will be calculated in optical fibres with RI of 1.35, 1.45, 1.55 and 1.65 respectively. The case for gold NPs in an optical adhesive and in fused silica optical fibre will be calculated specifically and the former will be demonstrated experimentally. Finally, as the formula for the calculation of the resonance wavelength shift is complex and time-consuming, a simplified analytic formula will be used, which is based on the formula for small NP extinction cross section, but only considering its main factors, in order to show the wavelength shift tendency.

2. Theory

Fig. 1 shows the modelled structure. 100nm size gold NPs are doped inside the core of the optical fibre over a short distance (several millimetres length). To make it clear, there is only one NP shown in the figure to illustrate the theory of the sensing method. Cartesian coordinates are defined as shown in Fig. 1. The Z axis is along the optical fibre and it is also the light transmission direction. The electrical field of the incident light is defined to be along the X direction.

Light is emitted from a broad band visible light source (for example a

halogen lamp to cover the light wavelength range of the plasmon resonance of the NPs) and then light is coupled into the left side of the optical fibre. The gold NP is shown in Fig. 1 in blue. The original status (without strain change) of the sensor is shown, not to scale, in Fig. 1(a). The shape of the NP is spherical with a radius R (50nm). Fig. 1(b) shows the case of the sensor under axial strain. The length of the optical fibre is changed from l to $l + \Delta l$. If the material property of the optical fibre is isotropic and the gold NP is also approximated as an isotropic material because the elastic anisotropy index of gold is small [34], then the spherical gold NP changes its shape to a spheroidal NP. The half axis of the spheroid along the optical fibre changes from R to $R_z \equiv R + \Delta R_z$. The half axis along the X and Y axis have the same values as $R_x = R_y$ and $R_x \equiv b \equiv R + \Delta R_x$ and $R_y \equiv c \equiv R + \Delta R_y$. $\Delta R_x = \Delta R_y$ and $b = c$.

Light will be extinguished by the NPs which induces the plasma resonance peak due to the LSPR. The LSPR is caused by the coherent oscillation of free electrons[22,35] and it changes when the shape of the NP change[22,36]. The propagating light after extinction is then detected by a spectrometer which is connected to the right side of the optical fibre. By determining the peak wavelength shift of the absorbance spectra, strain change values may be obtained.

To describe the shape change of the NP clearly in the optical fibre, the relative strain change along the optical fibre (α) between the NP and the optical fibre is defined as:

$$\alpha = \frac{\Delta R_z}{R} \frac{\Delta l}{l}. \quad (1)$$

The shape change of the NP (β) is defined as:

$$\beta = \frac{\Delta R_t}{\Delta R_z}, \quad (t = x, y), \quad (2)$$

which is similar to the definition of the Poisson's ratio [37].

The shape and the RI change of the NPs will induce the plasmon resonance peak change. In addition, the plasmon resonance peak is also influenced by the RI of the optical fibre. Therefore, the peak wavelength shift of the absorbance spectra under strain is a formula including these parameters.

To describe the influence by these parameters, in the following paragraphs, the RI for gold NP, the RI change of gold NP based on the modified LD model under strain change and the plasmon resonance wavelength and the wavelength shift under strain change will be analysed. The reason for using the LD model is that the LD model is a sum of the expressions of the oscillators and may generate a simpler analytic equation for the spectra shift under strain.

2.1. Modified Lorentz-Drude model for gold NP under strain change

Two parts constitute the permittivity of gold. They are free charge

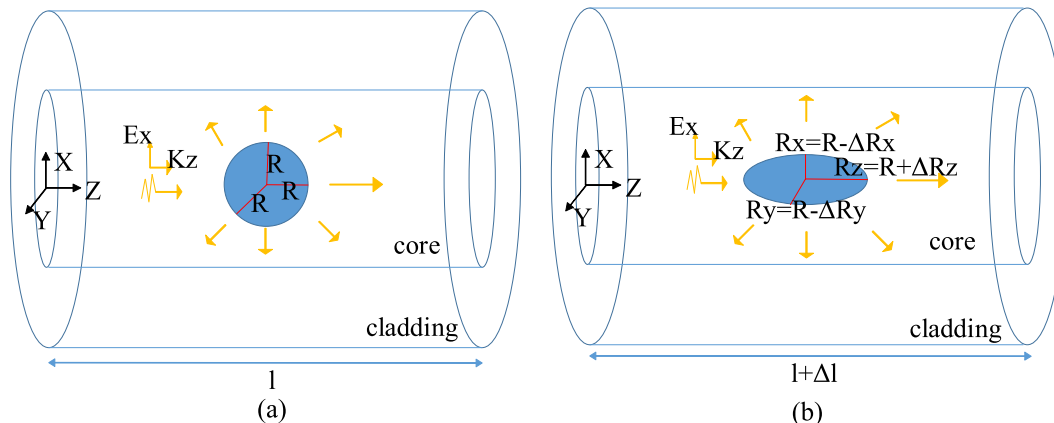


Fig. 1. Light extinction by the gold NP in the optical fibre. (a) Case of original status. (b) Case of strain change.

component (ϵ_{free}) and bound charge component (ϵ_{bound})[36]. The permittivity of gold can be expressed as:

$$\epsilon_{Au} = \epsilon_{free} + \epsilon_{bound}. \quad (3)$$

For nanometer size gold NPs, Scaffardi et al.'s model has a good match with the experimental data for nanometer size gold NPs as low as 0.6nm diameter gold NP[38] and also has a good match with the RI of bulk gold. See the experimental data from Johnson and Christy's experiment [39](blue stars) and the RI calculated by Scaffardi et al.'s model (red solid lines) shown in Fig. 2. n is the real part of the RI and k is the imaginary part of RI. The red dashed lines show the real and imaginary part of RI of 100nm size gold NP to give an intuitive deviation of RI for small size of gold and the deviation becomes smaller when the size of the NPs increases.

With Scaffardi et al.'s model the free charge component of the permittivity of gold can be expressed as:

$$\epsilon_{free}(\omega) = 1 - \frac{\omega_p^2}{\omega^2 + i(\gamma_{bulk} + H\frac{v_F}{R})\omega}, \quad (4)$$

where, ω is the angular frequency of light in vacuum, ω_p is the bulk plasma frequency of gold, γ_{bulk} is the damping constant for free electrons, H is a scattering constant, v_F is the electron velocity at the Fermi surface, and R is the radius of the gold particle[21,38]. Eq. (4) is an expression about R and ω . Fig. 3(a) and (b) show the deviation of the real part of free charge component of the permittivity and imaginary part of free charge component of the permittivity to the free charge component of the permittivity bulk gold respectively. The imaginary part is more influenced by the radius R compared with the real part.

The bound charge component of the permittivity of gold can be expressed as

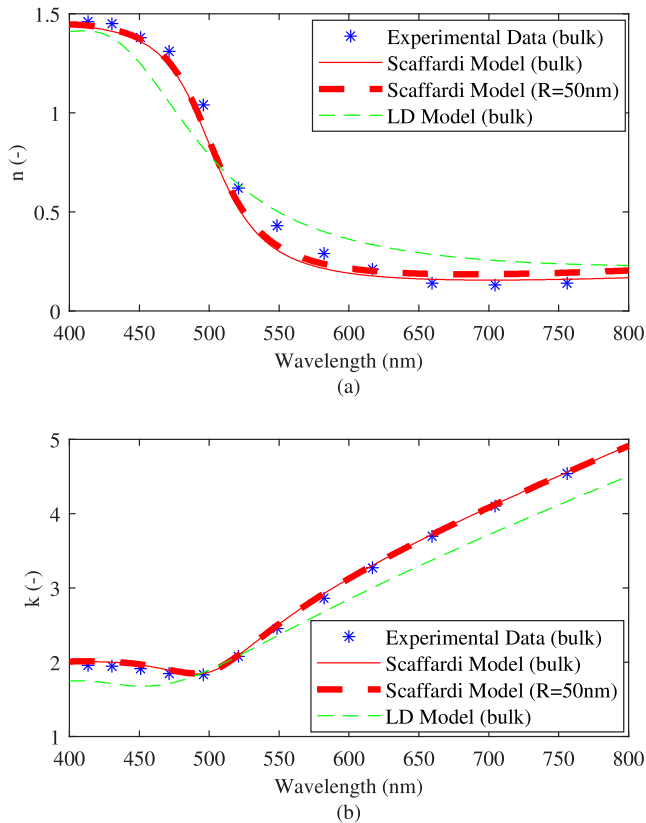


Fig. 2. The RI of gold. (a) The real part of the RI (n). (b) The imaginary part of the RI (k).

$$\epsilon_{bound}(\omega) = Q_{bulk}[1 - \exp(-\frac{R}{R_0})]G(\omega), \quad (5)$$

where,

$$G(\omega) = \int_{\omega_g}^{\infty} \frac{\sqrt{\omega' - \omega_g}}{\omega'} [1 - F(\omega', T)] \frac{\omega'^2 - \omega_g^2 + \gamma_b^2 + i2\omega\gamma_b}{(\omega'^2 - \omega_g^2 + \gamma_b^2)^2 + 4\omega^2\gamma_b^2} d\omega', \quad (6)$$

where, the parameter $Q_{bulk} = 2.3 \times 10^{24}$, ω' is the angular frequency in the integral equation, $R_0 = 0.35\text{nm}$, $\omega_g = 3.19 \times 10^{15}\text{Hz}$ is the angular frequency of the gap energy of gold, $F(\omega, T)$ corresponds to the Fermi energy distribution, k_b is the Boltzmann constant, $E_f = 2.5\text{eV}$ is the Fermi energy and γ_b corresponds to the damping constant of bound electrons of gold (refer to[21,38]).

The bound charge component of the permittivity of gold is an formula with R and ω (see Eqs. 5 and 6). However, the modification caused by R is quite small for large size NPs (>100nm diameter) and the modification of $(1 - \exp(-\frac{R}{R_0}))$ is less than $9.08 \times 10^{-61}\%$ because R_0 is only 0.35nm and the bound charge component will change only when the diameters of the NP are in the several nanometer or smaller size. For example, when the size of the gold NP is 1nm, this modification is about 76.0%. Therefore, the influence of the bound charge component of the permittivity caused by R can be neglected compared with the deviation of the free charge component (see Fig. 3). As shown in Fig. 2, the RI of the gold NP with diameter of 100nm calculated from the permittivity via Scaffardi's model is close to the RI of bulk gold. Therefore, the permittivity may vary for different radii of NPs can be expressed as:

$$\epsilon_{Au}(R, \omega) = \epsilon_{free}(R, \omega) + \epsilon_{bound}(\omega), \quad (7)$$

However, the Scaffardi et al.'s model was not chosen to obtain the approximate analytical expression of the spectral peak shift in this paper because the bound charge component of the permittivity is complicated. The simpler model, LD model, assuming the bound charge component of the permittivity is caused by a lot of oscillators[36] was used for the concise expression. According to the LD model, for bulk gold the permittivity of gold can be expressed as [40]:

$$\epsilon_{Au-LD} = 1 - \frac{f_0\omega_{p0}^2}{\omega(\omega + i\Gamma_0)} + \sum_{j=1}^k \frac{f_j\omega_{p0}^2}{(\omega_j^2 - \omega^2) - i\omega\Gamma_j}, \quad (8)$$

where ω_{p0} is the plasma frequency of gold, ω is the angular frequency of the incident light in vacuum, ω_j is the resonance frequency of the j th oscillator, Γ_0 is the damping constant of the free electron, Γ_j is the damping constant of the j th oscillator. f_0 and f_j can be obtained by fitting the experimental permittivity data. The tendency of the RI also matches well with the experimental data (see Fig. 2 blue stars and green dashed lines).

When the R equals infinite large, the bound charge component of the permittivity can be expressed as:

$$\epsilon_{bound}(\omega) = \epsilon_{Au-LD} - \epsilon_{free}(R \rightarrow \infty), \quad (9)$$

where,

$$\epsilon_{free}(R) = 1 - \frac{\omega_p^2}{\omega^2 + i\gamma(R)\omega}, \quad (10)$$

where, ω_p is the plasma frequency of gold and γ is the damping constant of the free electron,

$$\gamma(R) = \gamma_0 + A \frac{v_F}{L_{eff}(R)}, \quad (11)$$

and

$$L_{eff}(R) = 4 \frac{V}{S} = \frac{4R}{3}, \quad (12)$$

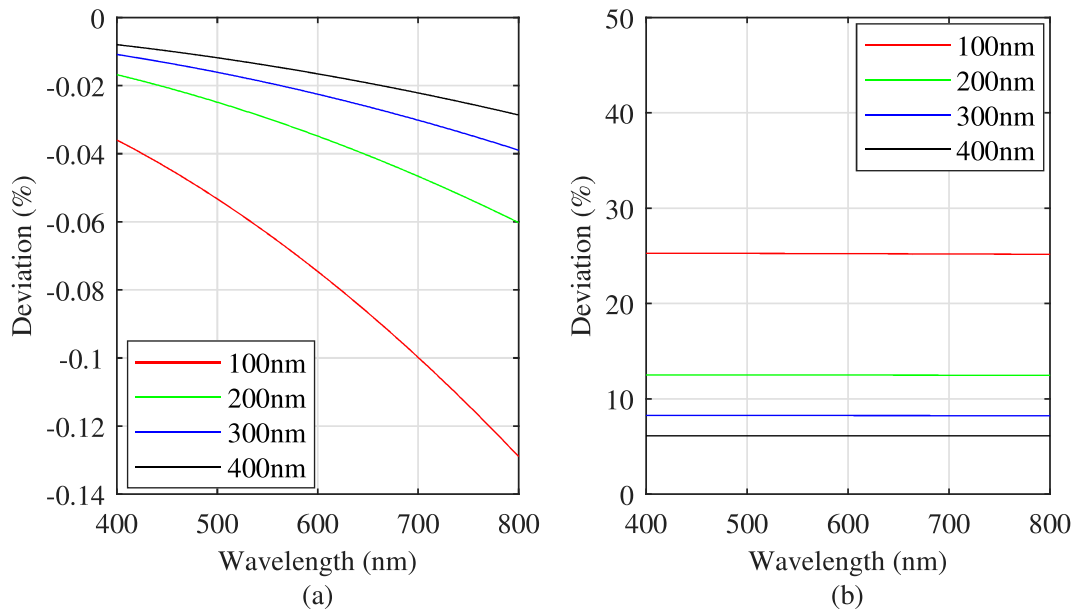


Fig. 3. The deviation of contribution of the permittivity of free-charge between gold NP and bulk gold. (a) The deviation of the real part. (b) The deviation of the imaginary part.

where, V is the volume of the NP and S is the surface area of the NP. When the strain changes, the shape of the spherical NP will become spheroidal and the density of the electrons will change. The plasma frequency is related to the electron density,

$$\omega_p = \sqrt{\frac{Ne^2}{\epsilon_0 m_{eff}}} \quad (13)$$

where, N is the electron density, e is the electron charge, ϵ_0 is the vacuum dielectric constant and m_{eff} is the effective electron mass. ν_F can also be influenced by the electron density as

$$\nu_F = \sqrt{\frac{2E_F}{m}} \quad (14)$$

where

$$E_F = \frac{\hbar^2}{2m} \left(\frac{3}{8\pi} \right)^{2/3} N^{2/3} \quad (15)$$

\hbar is the Planck constant, E_F is the Fermi energy, m is the mass of electron and for face centred cubic (FCC) structure metals.

$$N = \frac{4}{a_0^3} \quad (16)$$

where a_0 is the lattice constant of gold [29], which corresponds to the electron density before strain change. When the volume ratio is introduced to describe the density change, the electron density under strain change becomes:

$$N' = N \times \frac{V}{V'} \quad (17)$$

where V' is the volume of the gold NP under strain and $V' = 4\pi abc/3$. The surface area of the gold NP becomes $S' = 4\pi(ab + bc + ac)/3$. The strain will not only change the permittivity of the free-charge contribution but it will also change the permittivity of the bound-charge of the NP because of the electron density change[29]. Therefore, Eq. (9) needs to be modified by strain as:

$$\epsilon_{bound}(\omega) = \epsilon_{core}(\omega) - 1, \quad (18)$$

and ϵ_{core} is replaced by ϵ_c when the shape of the NP change:

$$\epsilon_c(\omega) = \frac{\epsilon_{core}(\omega) + 2 + 2\nu(\epsilon_{core}(\omega) - 1)}{\epsilon_{core}(\omega) + 2 - \nu(\epsilon_{core}(\omega) - 1)}, \quad (19)$$

where ϵ_{core} is the permittivity of the core part and the volume change ratio $\nu = R^3/abc$.

Therefore, by introducing strain related permittivity components, the modified LD model under strain change may eventually be expressed as:

$$\epsilon_{Au}(R) = \epsilon_{free}(R) + \epsilon_c(\epsilon_{core}) - 1, \quad (20)$$

where,

$$\epsilon_{core} = \epsilon_{Au-LD} - \epsilon_{free}(R \rightarrow \infty). \quad (21)$$

2.2. Plasmon resonance wavelength shift of gold NP

By acquiring the wavelength of the extinction cross section (C_{ext}), the plasmon resonance wavelength can be obtained. The extinction cross section of the NP can be calculated by Mie theory for spherical NPs [36] or by the T-matrix method for spheroidal NPs [41,42,33].

According to Mie theory [36], for a spherical particle,

$$C_{ext} = \frac{2\pi}{k^2} \Re \sum_n (2n+1)(a_n + b_n), \quad (22)$$

where, k is the wave vector in the medium. \Re is the symbol of the real part, and a_n and b_n are the scattering coefficients.

The T-matrix method also expands the field in terms of vector spherical wave function which is similar to Mie theory [33]. By constituting the relationship between the incident wave and the scattering wave with the matrix T as[43]:

$$\begin{bmatrix} p_\nu \\ q_\nu \end{bmatrix} = T \begin{bmatrix} a_\nu \\ b_\nu \end{bmatrix}, \quad (23)$$

where, p_ν and q_ν are the coefficients of the expanded scattered wave, a_ν and b_ν are the coefficients of the expanded incident wave, the subscript $\nu = (m, n)$ and $|m| \leq n$. and solving matrix T by integrating the vector spherical function on the particle's surface[44], the scattering and

absorption by the NP can be calculated. According to the T-matrix method for a spheroidal particle [41],

$$C_{ext} = \frac{-1}{k^2} \sum_{\nu} (p_{\nu}^* a_{\nu} + q_{\nu}^* b_{\nu}), \quad (24)$$

For more information about solving Eq. (24) and T-matrix refer to [41].

The method of using the T-matrix method along with fitting the plasmon resonance wavelengths under different strains values to obtain the peak shift values is generally time-consuming. Therefore, the high performance computing (HPC) cluster of the Aerospace Structures and Materials (ASM) department of Delft University of Technology was used to accelerate the calculation. The aimed NPs sizes are relatively small (100nm) when compared with the incident visible light wavelengths (around 600nm), so in the following part the small size assumptions for the extinction of the NPs are used in order to attempt to obtain a simpler analytical solution of the plasmon resonance wavelength shift.

Calculating the spectrum of the extinction of the spheroidal NPs is generally time-consuming under different strain values even with HPC clusters with T-matrix method. However, the size of NPs considered in this paper (100nm) is smaller compared with the incident wavelengths (>500nm). In this circumstance, the small extinction cross section may be used to simplify the calculation by deriving an approximate analytical expression to achieve fast calculation.

For small spheroidal NPs [36] ($b = c$) compared with the incident light, the polarizabilities α_1 and α_2 for parallel X axis and Y axis electrical field can be expressed as

$$\alpha = \alpha_1 = \alpha_2 = 4\pi abc \frac{\epsilon_{Au} - \epsilon_m}{3\epsilon_m + 3L(\epsilon_{Au} - \epsilon_m)}, \quad (25)$$

where, $L = 1/3$ for a spherical NP [36]. For small size NPs, the extinction cross section may be expressed as

$$C_{ext} = k\Im(\alpha) = 4\pi abc k\Im\left(\frac{\epsilon_{Au} - \epsilon_m}{3\epsilon_m + 3L(\epsilon_{Au} - \epsilon_m)}\right), \quad (26)$$

where, \Im is the symbol of the imaginary part.

When $\Re[3\epsilon_m + 3L(\epsilon_{Au} - \epsilon_m)] = 0$, the approximate plasmon resonance frequency, is obtained by solving the equation

$$\Re\epsilon_{Au}(\omega_{Fv}) = \epsilon_m \left(1 - \frac{1}{L}\right), \quad (27)$$

where ϵ_m is the permittivity of the medium which can be expressed as

$$\epsilon_m = \epsilon_{m0} \left(1 + \eta \frac{\Delta L}{L}\right)^2, \quad (28)$$

and η is the strain induced RI change of the medium.

The solution of Eq. (27) is ω_{Fv} which is the well-known Fröhlich frequency if $\Re\epsilon_{Au}$ satisfies Eq. (27) and $\Im\epsilon_{Au} \approx 0$. For a spherical NP with $L = 1/3$, Eq. (27) changes to $\Re\epsilon_{Au} = -2\epsilon_m$.

When the strain changes, the spectral peak calculated by Eq. 27 will shift. Eq. 27 is an implicit function of the spectral peak wavelength and the strain. The derivative of wavelength shift under strain can be calculated from the implicit function as a function of F

$$F = \Re\epsilon_{Au}(R) - \epsilon_m \left(1 - \frac{1}{L}\right). \quad (29)$$

Then, the peak wavelength shift can be obtained from

$$\left[\frac{d\omega}{dl/l}\right]_{\omega_{Fv}} = - \left[\frac{dF/(dl/l)}{dF/d\omega}\right]_{\omega_{Fv}}, \quad (30)$$

in angular frequency or can be expressed in wavelength as

$$\left[\frac{d\lambda}{dl/l}\right]_{\lambda_0} = \left[\frac{\lambda^2}{2\pi c'} \frac{dF/(dl/l)}{dF/d\omega}\right]_{\lambda_0}, \quad (31)$$

where c' the velocity of light in vacuum. The further approximation of Eqs. 30 and 31 are shown in the Results sections (see Eqs. (33)–(35)).

3. Methods

3.1. Experimental methodology

Gold NP suspension (100nm NP diameter, stabilized suspension in citrate buffer, 3.45×10^9 - $4.22 \times 10^9 \text{ml}^{-1}$, Sigma Aldrich) was put into a plastic tube and the water was evaporated at about 80°C . When the liquid of the gold NP suspension had been evaporated, 1ml optical adhesive (146H, Norland Products) was added to the tube and then stirred by an ultrasonic processor (750 Watt, Cole-Parmer) for 3min. During each minute the ultrasonic processor worked for 5sec with 30% of its total power. After the stirring process, part of the gold NP suspension was mixed into the optical adhesive. The optical adhesive containing gold NPs was then dropped onto two optical fibre end tips and cured by ultraviolet light using an ultraviolet lamp (PH135 SX Super Xenon, LABINO AB). Fig. 4 shows a photo of the optical end tips part of the experimental setup with the optical adhesive cured by the ultraviolet lamp. A USB (universal serial bus) microscope was put beside the optical fibre end tips to view the position change of the optical fibre end tips under pressure. The optical fibre end tips were made by connectors (30640G3, ϕ 640 μm bore, Thorlabs) with multimode optical fibre (FP600ERT, 0.50 NA, ϕ 600 μm core, Low OH, Thorlabs) and were fixed on a 3-axis stage (MAX373D, Thorlabs). The upper optical fibre was connected to a broad band light source (Tungsten Halogen light source, Ocean Optics). The light propagated along the optical fibre to the upper optical fibre end tip and then went through the optical adhesive to the lower optical fibre and was finally detected by a spectrometer (Cobra Vis, Wasatch Photonics, about 100pm resolution). When adjusting the Z direction along the optical fibre, the upper optical fibre end tip lowered its position and the lower optical fibre was fixed, so the cured optical adhesive was slightly compressed. Obtaining the spectrum without sample compression is used as the reference spectrum to obtain the peak absorbing wavelength. Then compressing the cured optical adhesive in Z direction and obtaining the corresponding absorbing spectra. By analysing the absorbance peak wavelengths obtained by the spectrometer under compression, the relationship between the Z displacement and the

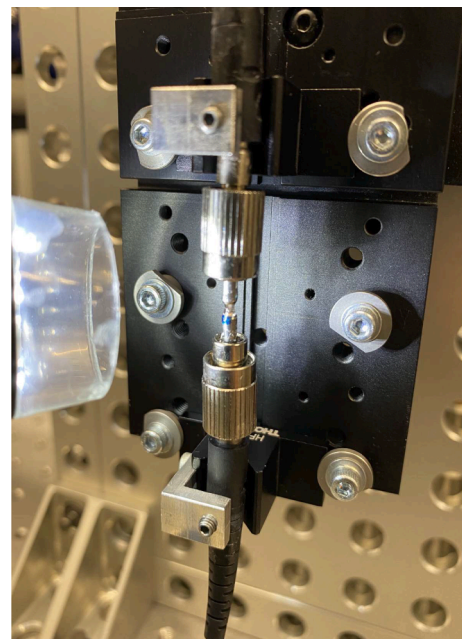


Fig. 4. Photo of the experimental setup..

absorbance peak wavelengths can be obtained. The accuracy of the position adjusting of the stage in Z direction is $1\mu\text{m}$. The relative positions of the two optical fibre end tips were recorded by reading the Z direction change from the stage. However, when the optical adhesive is in compression, the force on the optical adhesive will cause a deviation of the real relative positions of the two optical fibre end tips to the values read from the stage's micrometer, especially when the pressure is high. Therefore, a microscope was used to correct the relative position change. By obtaining the images from the microscope, the size of the ferrule of the optical fibre was obtained first for calibration. The relative positions of the two optical fibre end tips were then obtained by measuring the distances between the centres of the two end tips.

3.2. Numerical methodology

For the cases of 100nm size gold NPs in the optical adhesive and in the fused silica, the shape of the NP change was obtained using the finite element method (FEM) with the software Abaqus CAE 2019 (Dassault Systèmes). It is assumed that in the modelling region, there is only one NP and the NP is in the centre of model. The perfect contact condition was used for the interfaces of NPs and the optical fibre. The parameters of the spheroidal NP obtained from the FEM by Abaqus were then used for the simulation in the software MATLAB 2019a (The MathWorks) with the T-matrix method to calculate the extinction cross sections in visible light range around the plasmon resonance wavelengths on the HPC cluster. The plasmon resonance wavelengths under different strain values can be obtained using Eq. 24) to obtain the extinction spectrum first and then by fitting the peak of the spectra of the extinction cross section, the plasmon resonance wavelengths under different strain values can be obtained. The parameters for the calculation are shown in Table 1. The analytical results of the resonance wavelength shift were obtained using Eqs. 31 under small particle approximation.

4. Results

Fig. 5 shows the experimental and simulated results of the absorbance of 100nm size gold NP suspensions. The spectra of the absorbance of gold NP in citrate buffer (100nm diameter spherical gold NP, mean concentration $3.835 \times 10^9 \text{ml}^{-1}$), were obtained using a UV-Visible spectrometer (Lambda 35, Perkin Elmer), see the blue line in Fig. 5(a). The peak wavelength is 575nm. This was compared with the simulated results for the same concentration and size gold NPs with the modified LD model with T-matrix method, which is shown with a green dashed dot line (peak wavelength 579 nm) respectively, both simulated results match the experimental result well. The RI of the medium is set as 1.33 which is the same as the RI of water as the major component of citrate buffer is water. The Scaffardi et al. model [38] was also used as a comparison see the red dashed line (peak wavelength 562 nm).

The experimental results of the absorbance of gold NP suspension in the optical adhesive (Norland Optical Adhesive 146H, Norland Products, whose RI 1.46) is shown in Fig. 5(b) by a blue line. The gold NPs

Table 1
Parameters for calculation.

Parameters	Values	Parameters	Values
$\hbar\omega_{p_0}$	9.03eV [40]	f_5	4.384 [40]
$\hbar\omega_1$	0.415eV [40]	$\hbar\Gamma_0$	0.053eV [40]
$\hbar\omega_2$	0.830eV [40]	$\hbar\Gamma_1$	0.241eV [40]
$\hbar\omega_3$	2.969eV [40]	$\hbar\Gamma_2$	0.345eV [40]
$\hbar\omega_4$	4.304eV [40]	$\hbar\Gamma_3$	0.870eV [40]
$\hbar\omega_5$	13.32eV [40]	$\hbar\Gamma_4$	2.494eV [40]
f_0	0.760 [40]	$\hbar\Gamma_5$	2.214eV [40]
f_1	0.024 [40]	A	0.13 [29]
f_2	0.010 [40]	ν_F	$1.41 \times 10^6 \text{m/s}$ [29]
f_3	0.071 [40]	$1/\gamma_0$	$9.3 \times 10^{-15} \text{s}$ [29]
f_4	0.601 [40]	m_{eff}	$9.108 \times 10^{-31} \text{kg}$ [29]

have been mixed into the optical adhesive with ultrasonic stirring as mentioned in the Methods Section. Scaffardi et al.'s model [38] and the modified LD model are also used to show the simulated absorbance spectra with RI 1.46, which are shown by a red dashed line and a green dashed dot line respectively in Fig. 5(b) for the same mean gold NP concentration ($3.835 \times 10^9 \text{ml}^{-1}$). Note: due to the low percentage of gold NPs transferred to the optical adhesive, the simulated results have been multiplied by a factor of 0.02 in order to show the results in the same scale. The peak wavelength of the experimental result with polynomial fitting is 592 nm, which is close to the simulated results both from Scaffardi et al.'s model of 588 nm and from the modified LD model of 610 nm.

The simulated results with the T-matrix method have been compared with the solutions calculated by Mie theory and the errors between them are quite small. Within the wavelength range from 500 nm to 650 nm, the errors are less than 0.3%.

When moving the upper optical fibre end tip closer to the lower optical fibre end tip, as shown in Fig. 4, there is a compressive force on the cured optical adhesive containing gold NPs. Fig. 6 shows the experimental results of the transmittance and the absorbance for different position change values. The transmittance shown in Fig. 6(a) was obtained by dividing the transmitted light for the cured optical adhesive containing gold NPs by the intensity of the transmitted light intensity for only optical adhesive between the optical fibre end tips. The absorbance shown in Fig. 6(b) is obtained from the transmittance in Fig. 6(a). It can be seen from Fig. 6(b) that there is a blue shift when pressing the cured optical adhesive containing gold NPs.

Fig. 7(a) shows the peak wavelengths shift under compressive strain. The precision of obtaining the peak wavelengths depends on the method used for tracking the spectral peak and the noise level of the spectrum. In this work, the peak wavelengths were obtained from the polynomial fittings. In order to reduce the influence of the noise on the peak values, the data were averaged by measurements. By averaging the data from multiple measurements, a more precise peak wavelength can be obtained. 50 measurements were used to check the deviation of the peak wavelength values obtained by polynomial fitting and the standard deviation is about 191.2pm. The data shown in Fig. 7 are the peak wavelengths obtained by the 8-order polynomial fittings with 400 measurements. In Fig. 7(a), the blue dots show the peak wavelengths with their position change values read directly from the 3-axis stage. The red dashed line shows the linear fit of the blue dots for a position change range from $0\mu\text{m}$ to $100\mu\text{m}$ in the yellow region of Fig. 7(a). The gradient of the fitting curve is $0.0464 \text{nm}/\mu\text{m}$. It can be seen from Fig. 7(a) that the gradient is reduced for a larger position change. This is because the lower optical fibre cannot stand too much force when the compressive force is high. The lower optical fibre's position will also move slightly. In order to reduce the effect from this movement, a microscope was used for the distance correction. The distance modification used two measurements. One is the original distance, the other is when the readout position changed by $100\mu\text{m}$. Each was measured 6 times. The orange dots in Fig. 7(a) are the modified results. The gradient of its linear fitting curve is $0.1328 \text{nm}/\mu\text{m}$. The original distance between the two optical fibre end tips, before applying the compressive force, is $1.3505 \pm 0.0129 \text{mm}$ from the microscope. Based on the original distance, the peak wavelengths under different strain values were obtained as shown in Fig. 7(b). The red line is the linear fitting curve and its gradient is $-0.1915 \pm 0.1108 \text{pm}/\mu\text{m}$ with the peak wavelength 587.7nm at strain 0. As shown in Fig. 7(b), the dynamic range of the setup is from about -0.03ϵ to 0ϵ . It is a large dynamic range but the setup only can apply compression on the sample. The theoretical dynamic range depends on the material used as the optical fibre. For fused silica, the dynamic range can be up to 4% [45].

FEM has been previously used for the simulation of composites containing NPs [46] and the size of the NP is relatively large (100nm), therefore an FEM simulation with the software Abaqus was used to determine the shape change of gold NP in the optical adhesive. Although

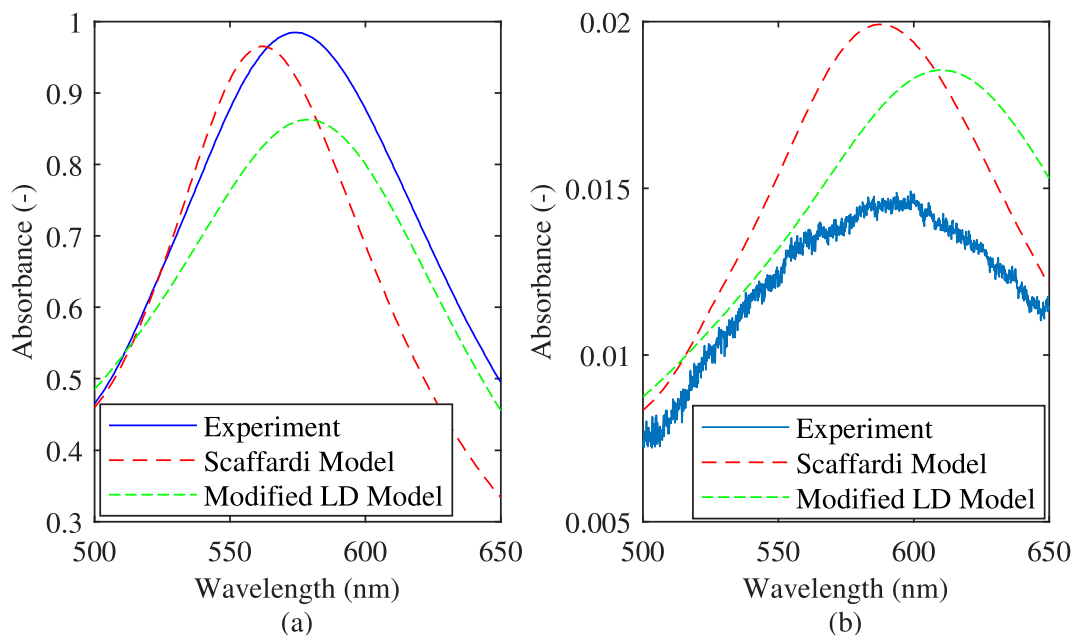


Fig. 5. Experimental and simulated results of the absorbance of 100nm size gold NP suspensions. (a) Gold NPs in water. (b) Gold NPs in the optical adhesive.

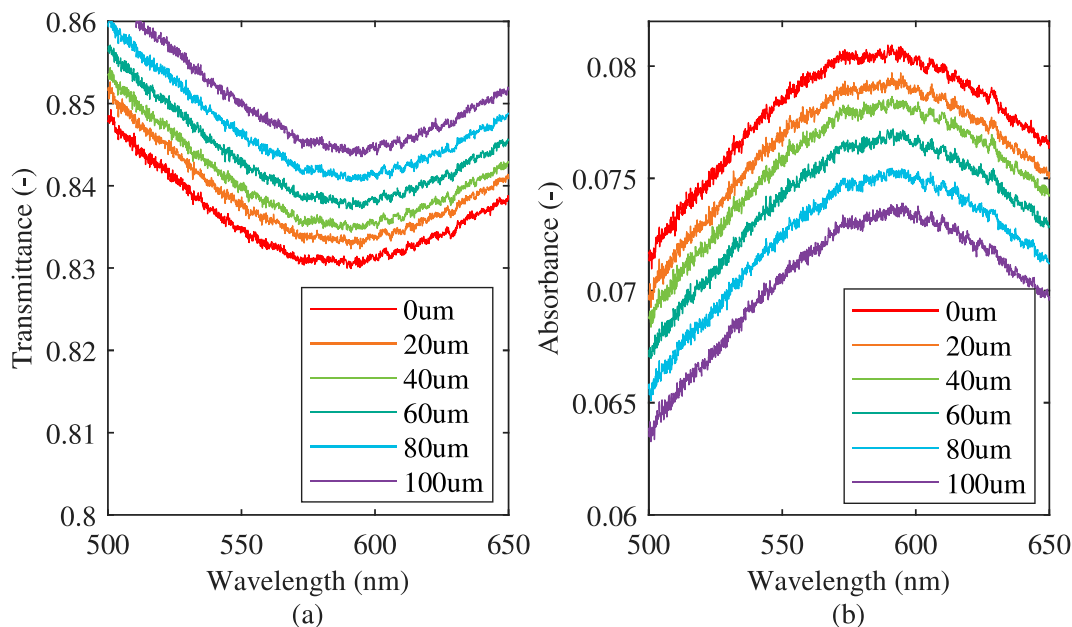


Fig. 6. Experimental results of the spectra of gold NP in the cured optical adhesive under pressure (the position change of the upper optical fibre end tip is read from a 3-axis stage directed as shown in the legend). (a) Transmittance. (b) Absorbance.

the simulated results will have an error due to the restriction of the small size of the NPs, the simulated results are expected to approximate the behaviour of the NPs inside the optical fibre under strain change. This mechanical behaviour of the optical fibre containing NPs needs to be verified by experiment.

Fig. 8 shows the structure for FEM simulation. The green region is the gold NP and the ivory white region is the optical adhesive. The NP is set in the middle of the cubic medium with 100nm diameter. The length of the cubic medium was set at 200nm. The boundary conditions were set as 0.5% position change at both left from face and right back face of the cubic under pressure. The Young's modulus of gold is 78nN/nm^2 . The Poisson's ratio of gold is 0.44 [47]. The Young's modulus of the medium (optical adhesive) is set as $10 \times 10^{-5}\text{nN/nm}^2$ as a typical value.

Poisson's ratio of the optical adhesive is 0.43. A high volume percentage of the NP to the medium could influence of the shape change of the NP. However, as shown in Fig. 9 for a the deformation scale factor of 1, the shape change of the NP in the optical adhesive is 5-orders smaller than the shape change of the optical adhesive. Therefore, the shape change of the NP in the optical adhesive can be neglected mechanically. By adjusting the RI change of the optical adhesive in the simulation to match the gradient of the peak wavelength shift of the experimental result, the corresponding RI change of the optical adhesive is $-0.52 \pm 0.28\text{ppm}/\mu\epsilon$.

A gold NP is expected to enhance the contrast ratio in the distributed sensing [21] for high sensitivity strain sensing. The case of a gold NP in fused silica is also calculated. Fig. 10 shows result of shape change of the

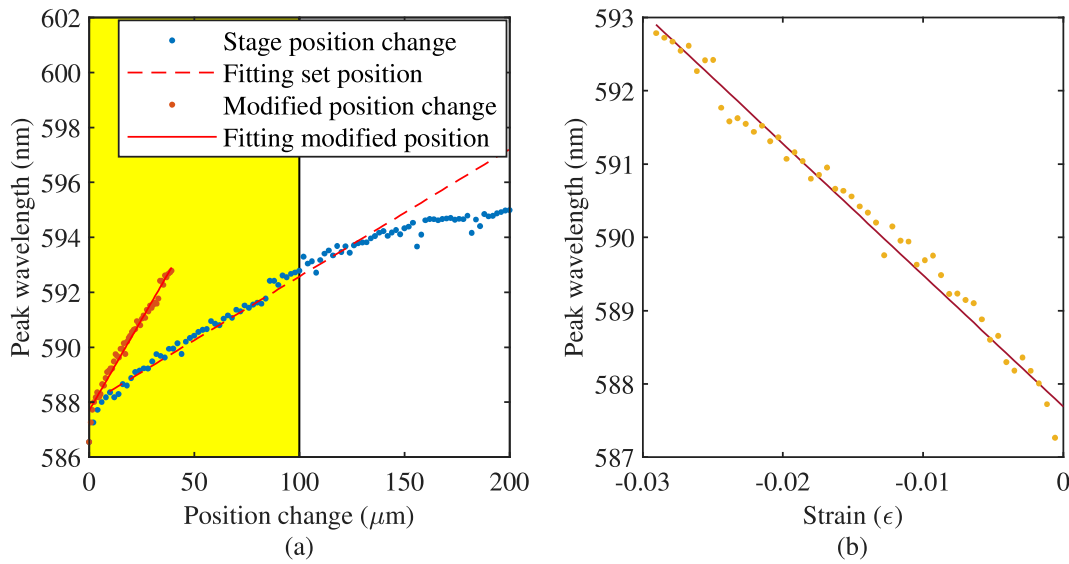


Fig. 7. Peak wavelength shift under pressure. (a) The original peak wavelength shift (blue dots) and the modified shift (orange dots) with their linear fitting curves. (b) Peak wavelength shift under different strain values with the linear fitting curve.

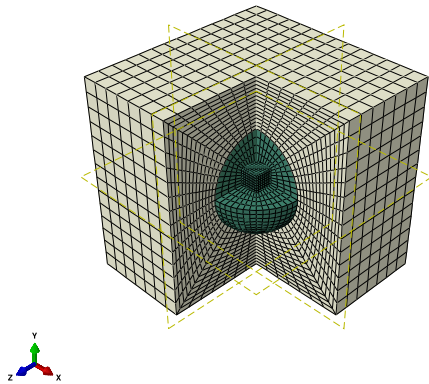


Fig. 8. The structure of medium containing gold NP for FEM simulation. Green region is the gold NP. Ivory white region shows the medium.

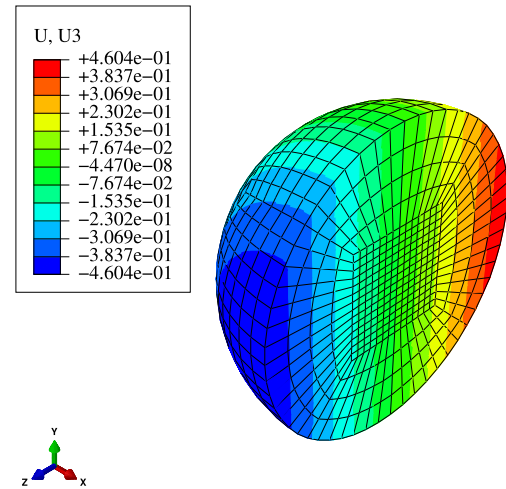


Fig. 10. The shape change of gold NP in fused silica along Z direction under pressure. (The displacement unit is nm).

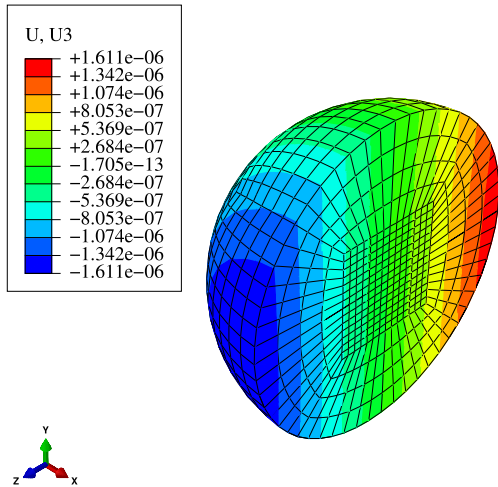


Fig. 9. The gold NP shape change in optical adhesive along Z direction under pressure. (The displacement unit is nm).

NP in the fused silica with the same structure shown in Fig. 9 but with the material of the optical fibre changed to fused silica. The Young's modulus of the medium (fused silica) used in FEM is $73\text{nN}/\text{nm}^2$ [48] and the Poisson's ratio is 0.17 [49].

It can be seen from Fig. 10 that the shape change of the gold NP is close to the shape change of the fused silica. The volume ratio of the gold NP to the medium also influences the shape change of the NP.

The RI change of fused silica can be taken into account in the T-matrix method by using the modified LD model to calculate the peak wavelength change ratio. The light propagating along the optical fibre sees the RI change of the fused silica is [50]

$$\Delta n = -\frac{1}{2}n^3[(1-\nu')p_{12} - \nu'p_{11}]\epsilon, \quad (32)$$

where, ν' is the Poisson's ratio for fused silica. For silica fibre at 633nm incident light, $p_{11} = 0.113$, $p_{12} = 0.252$, [51] The RI change is $-0.200\text{ppm}/\mu\epsilon$ when $n = 1.45$.

Fig. 11 shows the relative length change and the corresponding peak wavelength change ratio under different gold NP concentration by changing the FEM simulation model size, namely change the size of the

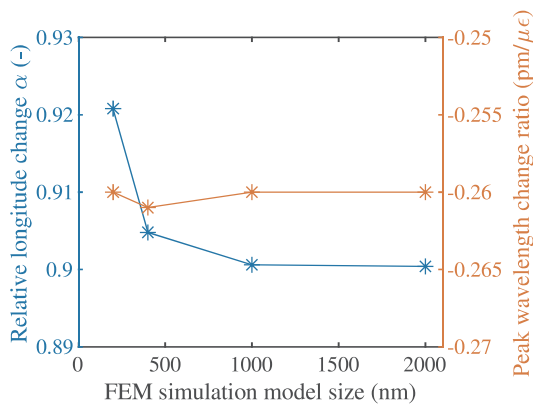


Fig. 11. The relationship of the relative axial length change of NP to optical fibre and peak wavelength change based on FEM for different simulation sizes.

medium. The length of the cubic medium was set at 200nm, 400nm, 1000nm and 2000nm respectively, which corresponds to concentrations of $1.25 \times 10^{14} \text{ml}^{-1}$, $1.56 \times 10^{13} \text{ml}^{-1}$, $1.25 \times 10^{12} \text{ml}^{-1}$ and $1.56 \times 10^{11} \text{ml}^{-1}$ respectively. When the concentration of the NP decreases, the relative axial length change (α) decreases and it becomes stable. From this point the peak wavelength change ratio is not influenced by the concentration change. For fused silica or some polymer materials, the RI range is in the range of 1.3 to 1.7. Fig. 12 shows 4 cases in this RI range with the RI of the optical fibre of 1.35, 1.45, 1.55 and 1.65 in Fig. 12(a) to (d). Fig. 12 is plotted based on the T-matrix method for a gold NP with the modified LD model under RI change of the medium (η) and NP shape change ratio (β) (with 116 Central Processing Units (CPUs) from the HPC cluster for about 1 day). The fitting wavelength range is from 550nm to 650nm. The wavelength interval is 0.1nm. The RI change is from $-10 \text{ppm}/\mu\epsilon$ to $10 \text{ppm}/\mu\epsilon$ with the interval of $0.5 \text{ppm}/\mu\epsilon$.

The NP shape change ratio is from -0.45 to -0.17 with the interval of 0.01. The peak wavelength change ratio is obtained by linear fitting of the peak wavelengths in a small strain range $-1000\mu\epsilon$ to $1000\mu\epsilon$ with the interval of $100\mu\epsilon$.

It can be seen from Fig. 12 that the RI change of the optical fibre is the main factor of the values of peak wavelength change ratio when compared with the NP shape change and shape change induced gold RI change as well. By comparing Fig. 12(a) to (d), it can be seen that when the RI of the medium increases the value of the peak wavelength change ratio becomes intense. The NP shape change will also modulate the peak wavelength change ratio slightly but it only becomes important when the RI change is around $0 \text{ppm}/\mu\epsilon$. The NP shape change in the range shown in Fig. 12 shows a blue shift of the peak wavelength change, which can be seen more clearly in the embedded graph in Fig. 12(b). As shown in the embedded graph in Fig. 12(b), the peak wavelength shifts are not zero when the RI change η (RI change of the optical fibre) is zero. Fig. 12(b) shows the peak wavelength shift caused by the morphing of the gold NPs in the optical fibres. The peak wavelength shifts are influenced by the NP shape change ratios. Some commercial optical fibres are manufactured based on fused silica (RI of about 1.45) for their low loss especially in the telecom optical wavelength bands. For an example, a red star is plotted in Fig. 12(b) to show that when the ratio of length change of the NP to axial fused silica is 0.9208, the RI change is $-0.216 \text{ppm}/\mu\epsilon$, which corresponds to concentrations of NPs of $1.25 \times 10^{14} \text{ml}^{-1}$. Note: Fig. 12 is plotted for relative strain change α between the optical fibre and the NP at 1. The advantage of using the factor 1 is that for other values of α it is simple to obtain the corresponding values by scaling. For examples, for other values of α , the RI change in Fig. 12 only needs to be multiplied by $1/\alpha$ and the final result needs to be multiplied by α to obtain the corresponding peak wavelength change ratio when the NP longitudinal length change is $1 \text{ppm}/\mu\epsilon$. Therefore, the value of the red star plotted on Fig. 12(b) is $-0.282 \text{ppm}/\mu\epsilon$ and after multiplication by α becomes $-0.260 \text{ppm}/\mu\epsilon$.

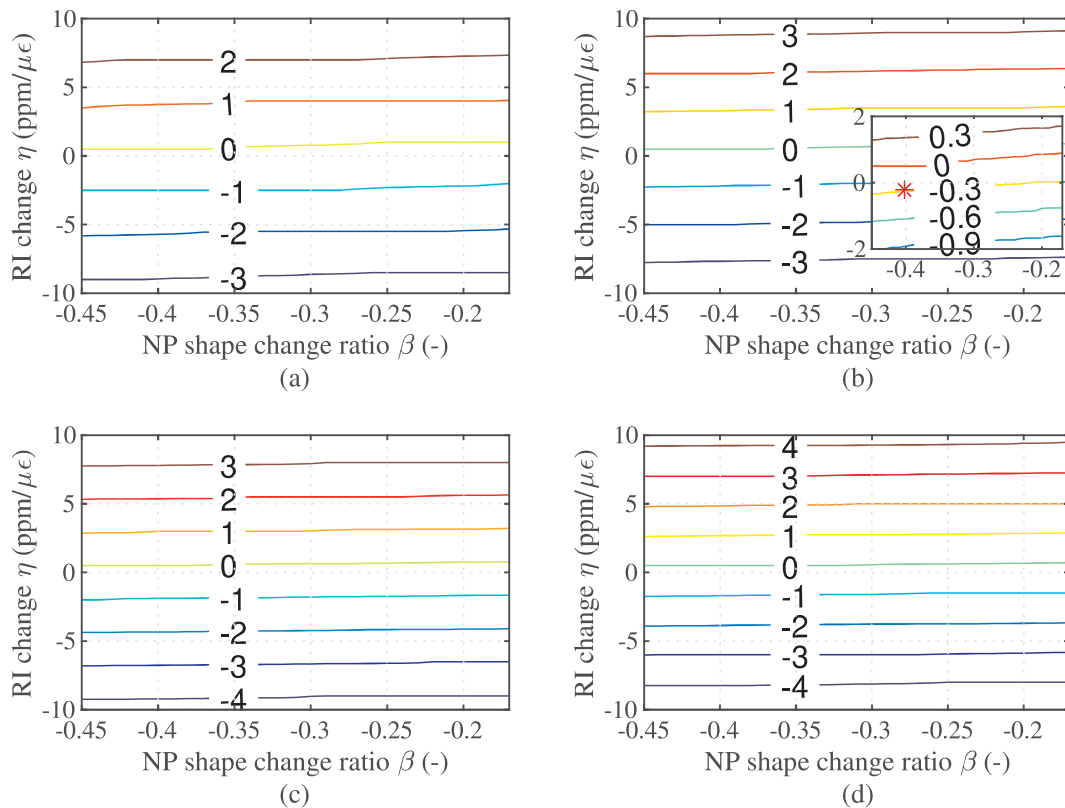


Fig. 12. The peak wavelength change ratio in small strain ($\pm 0.001\epsilon$ range linear fitting, $\alpha = 1$). The RI of the optical fibre in (a) - (d) are 1.35, 1.45, 1.55 and 1.65 respectively. The unit of the peak wavelength change ratio of the contour line is $\text{pm}/\mu\epsilon$.

Because the RI change of the optical fibre is the main factor of the values of peak wavelength change ratio, Eq. (31) may be simplified when the change of RI and shape of the NPs are not taken into consideration. Then, Eq. (31) may be simplified as

$$\left[\frac{d\lambda}{dI}\right]_{\lambda_0} = G \frac{\lambda_0^2}{2\pi c'} \frac{[dF/(dI/I)]_{\omega_{Fv}}}{[dF/d\omega]_{\omega_{Fv}}}, (G = 1) \quad (33)$$

where,

$$\left[\frac{dF}{(dI/I)}\right]_{\omega_{Fv}} = 4\epsilon_{m0}\eta. \quad (34)$$

and

$$\begin{aligned} \left[\frac{dF}{d\omega}\right]_{\omega_{Fv}} &= \frac{2\omega_p^2\omega_{Fv}}{(\omega_{Fv}^2 + \gamma^2)^2} + \frac{2f_0\omega_p^2\omega_{Fv}}{(\omega_{Fv}^2 + \Gamma_0^2)^2} + \sum_{j=1}^k \frac{2f_j\omega_{p0}^2\omega_{Fv}(\omega_j^2 - \omega_{Fv}^2)^2}{[(\omega_j^2 - \omega_{Fv}^2)^2 + \omega_{Fv}^2\Gamma_j^2]^2} \\ &- \sum_{j=1}^k \frac{2f_j\omega_{p0}^2\omega_{Fv}(\omega_j^2 - \omega_{Fv}^2)}{[(\omega_j^2 - \omega_{Fv}^2)^2 + \omega_{Fv}^2\Gamma_j^2]^2} + \sum_{j=1}^k \frac{f_j\omega_{p0}^2\omega_{Fv}^2\Gamma_j^2}{[(\omega_j^2 - \omega_{Fv}^2)^2 + \omega_{Fv}^2\Gamma_j^2]^2} - \frac{2\omega_p^2\omega_{Fv}}{(\omega_{Fv}^2 + \gamma_0^2)^2}. \end{aligned} \quad (35)$$

It can be seen from Eq. (34) that η determines the sign of the ratio. The results from Eqs. (33)–(35) are shown in Fig. 13 to make a comparison. The embedded graph shown in Fig. 13(b) shows the identical region shown in Fig. 12(b). The results become anti-symmetric around 0 because of the lacking of the influence caused by the RI change of gold. The red star is at the same position in Fig. 12(b). The approximated

plasmon resonance wavelengths were calculated based on Eq. (27). The features caused by the NP shape change are lost but the features caused by the RI change are maintained even though the values deviate from the values calculated by elaborated calculation shown in Fig. 12.

5. Discussion

The modified LD model has been compared with the experimental results and the Scaffardi et al.'s model in Fig. 5. The modified LD model not only matches the experimental results and the Scaffardi et al.'s model well for the spherical gold NP, but also can be used for the spheroidal NP under strain change. Compared with other methods, for example Scaffardi et al. model or the Brendel-Bormann model, it does

not exactly match the experimental results. However, the LD model has a simpler expression and its derivative function is more explicit in order to derive the analytic expression under strain change.

From the modified LD model in this paper, the plasmon resonance peak wavelength change ratio can be related to the shape change of the NP, the shape change induced RI change of the NP, the RI of the optical fibre and the RI change of the optical fibre. The Young's modulus and

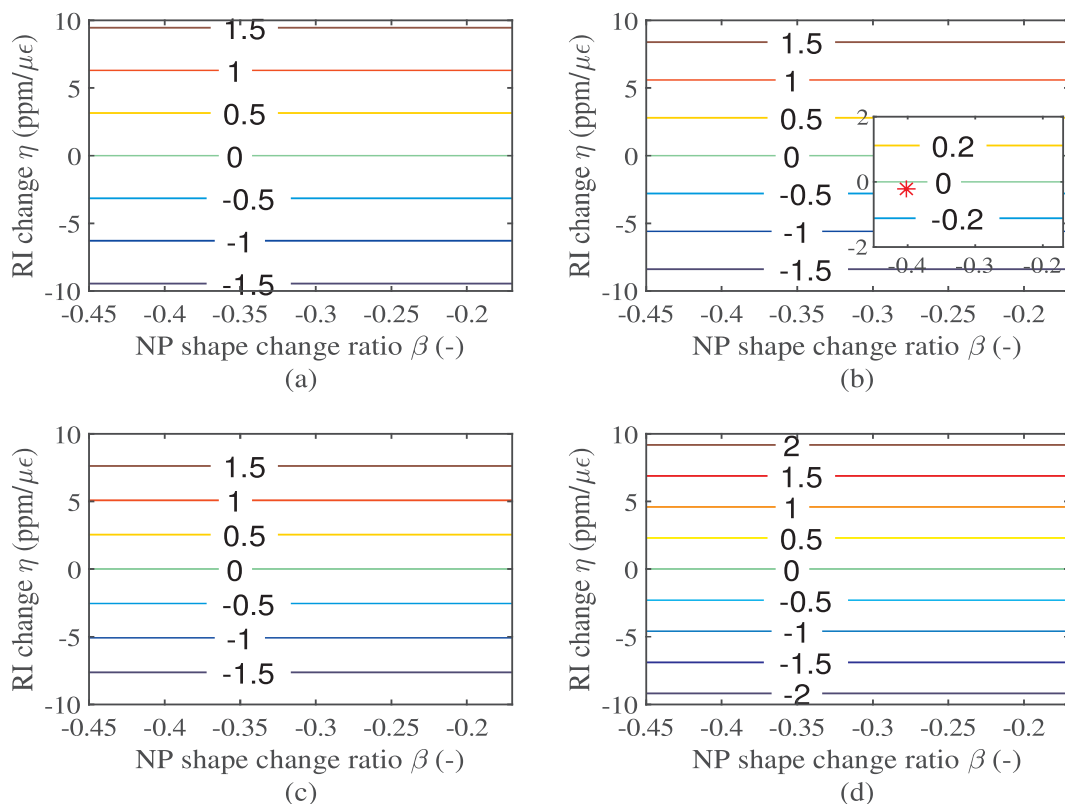


Fig. 13. Estimated peak wavelength change ratio. RI of the optical fibre in (a) - (d) are 1.35, 1.45, 1.55 and 1.65 respectively. The unit of the peak wavelength change ratio of the contour line is pm/ $\mu\epsilon$.

the Poisson's ratio and the concentration of the NP are also factors to adjust the values of the plasmon resonance peak wavelength change ratio. From Fig. 12, it can be seen that the RI change is the major factor to influence the peak wavelength change ratio. Therefore, by choosing different materials for the optical fibre, the sensitivity of the plasmon resonance peak wavelength change can be tuned.

For a commercial fused silica based optical fibre or fibre Bragg grating, the strain induced peak wavelength change is about $1.2\text{pm}/\mu\text{e}$ for about 1550nm incident light. If the optical fibre properties are modified, especially by introducing a higher RI and photo-elastic coefficient of the optical fibre, a high sensitivity of the plasmon resonance peak wavelength change may be achieved. Compared with those for infrared light, detectors for the visible light not expensive which is an advantage for the plasmon peak detection. For some metal NPs the plasmon peak is in the visible range.

In addition, the shape change of the NP will also change the peak wavelength change ratio, especially when the RI change is around 0. In this case, by choosing optical fibres with suitable Young's modulus and Poisson's ratio, the shape change of the NP can be tuned and then the peak wavelength change ratio can be tuned finely. Other face centred cubic materials for example silver, have a larger sensitivity based on its shape change.

The simplified analytic equation for calculating the peak wavelength shift under strain can show the trend, but the values deviates from the exact calculation results shown in Fig. 12 because the NP size is quite large. The calculated plasmon resonance wavelengths for RI of 1.35, 1.45, 1.55, 1.65 are 513 nm, 521nm, 537 nm, and 550 nm respectively, which are also deviates from the peak wavelengths by fitting. However, it can be found that the results in Fig. 13 match the results in Fig. 12 well when the approximated results multiples a factor (G) of about 2. This indicates that a larger size of gold NP has a larger peak wavelength change response to the axial strain change. From simulations of gold and silver NPs for larger sizes (larger than 100nm), the peak wavelength ratio will also increase slightly when the sizes of the NPs increase. Therefore, by using larger size of gold NPs, the sensitivity will increase. However, the width of the peak wavelength will also increase with may cause a difficulty in determining the peak wavelength values.

In this paper, gold NPs smaller than 100 nm diameter have not been taken into consideration. For 100nm size gold NP, there are a lot of atoms (about 245 atoms) along its diameter, so the Young's modulus and Poisson's ratio may be still appropriate for the calculation for this size safely. However, for smaller NPs especially several nanometer size NPs, the number of atoms is quite small and material parameters may vary from those of bulk materials, so for these small NPs this effect still needs to be investigated.

The temperature is also a factor which influences the strain sensing because the variation of temperature will cause the length change of the optical fibre and the RI change of both of the NPs and the optical fibre. This may cause a difficulty in decoupling the strain information and temperature information. In this paper, it is assumed that the room temperature is constant. Therefore, the influence of the variation of the temperature needs to be investigated in the future. It can be noticed that the strain detection channels of the plasmon resonance based strain sensing and the traditional distributed fibre optic sensing based on Rayleigh backscattering is different, using visible light channel and near infrared channel respectively. By combining these two methods, the strain information may be decoupled from the temperature variation. There is a remarkable advantages of doping gold NPs over other oxide materials or fused silica fibre without doping NPs. Gold NP doped optical fibres generate plasmon resonance. This makes it possible to provide additional strain information by obtain the plasmon resonance shift. However, the method of spectral peak tracking with polynomial fitting is sensitive to the noise. Therefore, methods to precisely track the spectral peaks and methods for depressing the noise level in the measurements still need to be investigated.

6. Conclusions

In this paper, a modified LD model was used to simulate the peak wavelength change under strain change. By experiment, the peak wavelength change under strain change has been observed. By simulation, the peak change has been then analysed for different RI to cover the range of fused silica and some polymer optical fibre materials of 100nm gold NP. The peak wavelength change ratio can be used for strain detection. By changing the shape of the NP, the type and size of the NP, and the materials of the optical fibre, the peak wavelength change ratio can be tuned. Therefore, a highly sensitively strain sensing may be achieved by plasmon resonance based gold NP doped optical fibre. Due to the sensing wavelength range being different from typical distributed fibre optic sensing based on Rayleigh scattering, it may be an auxiliary strain detection method along with distributed fibre optic sensing based on Rayleigh scattering.

Declaration of Competing Interest

The authors declare that they have no known competing financial interests or personal relationships that could have appeared to influence the work reported in this paper.

Acknowledgments

The authors gratefully acknowledge financial support from the China Scholarship Council (No. 201806020197) and thank Sybrand van der Zwaag and Johan Bijleveld for useful discussions, Michaël Maria for assistance with the spectrum acquisition, Nan Tao for assisting with the Abaqus simulation and Durga Mainali Sharma for assistance in the Chemistry Lab.

References

- [1] V. Giurgiutiu, 16 - Structural health monitoring (SHM) of aerospace composites, in: P. Irving, C. Soutis (Eds.), *Polymer Composites in the Aerospace Industry*, Woodhead Publishing, 2015, pp. 449–507.
- [2] J. Ou, H. Li, Structural health monitoring in mainland china: review and future trends, *Struct. Health Monit.* 9 (3) (2010) 219–231.
- [3] J.D. Achenbach, Structural health monitoring—what is the prescription? *Mech. Res. Commun.* 36 (2) (2009) 137–142.
- [4] A. Kesavan, S. John, I. Herszberg, Strain-based structural health monitoring of complex composite structures, *Struct. Health Monit.* 7 (3) (2008) 203–213.
- [5] H. Rocha, C. Semprinoschnig, J.P. Nunes, Sensors for process and structural health monitoring of aerospace composites: A review, *Eng. Struct.* 237 (2021) 112231.
- [6] Y. Huang, L. Liu, F. Sham, Y. Chan, S. Ng, Optical strain gauge vs. traditional strain gauges for concrete elasticity modulus determination, *Optik* 121 (18) (2010) 1635–1641.
- [7] S. Liu, Y. Wang, C. Liao, G. Wang, Z. Li, Q. Wang, J. Zhou, K. Yang, X. Zhong, J. Zhao, J. Tang, High-sensitivity strain sensor based on in-fiber improved Fabry-Pérot interferometer, *Opt. Lett.* 39 (7) (2014) 2121–2124.
- [8] A. Rajabzadeh, R. Heusdens, R.C. Hendriks, R.M. Groves, Characterisation of transverse matrix cracks in composite materials using fibre Bragg grating sensors, *J. Lightwave Technol.* 37 (18) (2019) 4720–4727.
- [9] M. Mieloszyk, K. Majewska, W. Ostachowicz, Application of embedded fibre Bragg grating sensors for structural health monitoring of complex composite structures for marine applications, *Mar. Struct.* 76 (2021) 102903.
- [10] N. Nazeer, R.M. Groves, Load monitoring of a cantilever plate by a novel multimodal fibre optic sensing configuration, *SN Appl. Sci.* 3 (6) (2021) 1–17.
- [11] C. Liang, Q. Bai, M. Yan, Y. Wang, H. Zhang, B. Jin, A comprehensive study of optical frequency domain reflectometry, *IEEE Access* 9 (2021) 41647–41668.
- [12] T. Wu, G. Liu, S. Fu, F. Xing, Recent progress of fiber-optic sensors for the structural health monitoring of civil infrastructure, *Sensors* 20 (16) (2020) 4517.
- [13] R. Di Sante, Fibre optic sensors for structural health monitoring of aircraft composite structures: Recent advances and applications, *Sensors* 15 (8) (2015) 18666–18713.
- [14] H. Guo, G. Xiao, N. Mrad, J. Yao, Fiber optic sensors for structural health monitoring of air platforms, *Sensors* 11 (4) (2011) 3687–3705.
- [15] R. Sienko, M. Zych, L. Bednarski, T. Howiacki, Strain and crack analysis within concrete members using distributed fibre optic sensors, *Struct. Health Monit.* 18 (5–6) (2019) 1510–1526.
- [16] A. Barrias, J.R. Casas, S. Villalba, A review of distributed optical fiber sensors for civil engineering applications, *Sensors* 16 (5) (2016) 748.
- [17] D. Tosi, C. Molardi, W. Blanc, Rayleigh scattering characterization of a low-loss MgO-based nanoparticle-doped optical fiber for distributed sensing, *Opt. Laser Technol.* 133 (2021) 106523.

- [18] V. Fuertes, N. Grégoire, P. Labranche, S. Gagnon, R. Wang, Y. Ledemi, S. LaRochelle, Y. Messaddeq, Engineering nanoparticle features to tune Rayleigh scattering in nanoparticles-doped optical fibers, *Sci. Rep.* 11 (1) (2021) 1–12.
- [19] A. Beisenova, A. Issatayeva, I. Iordachita, W. Blanc, C. Molardi, D. Tosi, Distributed fiber optics 3D shape sensing by means of high scattering NP-doped fibers simultaneous spatial multiplexing, *Opt. Express* 27 (16) (2019) 22074–22087.
- [20] A. Beisenova, A. Issatayeva, S. Korganbayev, C. Molardi, W. Blanc, D. Tosi, Simultaneous distributed sensing on multiple MgO-doped high scattering fibers by means of scattering-level multiplexing, *J. Lightwave Technol.* 37 (13) (2019) 3413–3421.
- [21] X. Wang, R. Benedictus, R.M. Groves, Optimization of light scattering enhancement by gold nanoparticles in fused silica optical fiber, *Opt. Express* 29 (13) (2021) 19450–19464.
- [22] S. Jayabal, A. Pandikumar, H.N. Lim, R. Ramaraj, T. Sun, N.M. Huang, A gold nanorod-based localized surface plasmon resonance platform for the detection of environmentally toxic metal ions, *Analyst* 140 (8) (2015) 2540–2555.
- [23] C. Shen, Y. Zhang, W. Zhou, J. Albert, Au-coated tilted fiber Bragg grating twist sensor based on surface plasmon resonance, *Appl. Phys. Lett.* 104 (7) (2014) 071106.
- [24] X. Zhang, J. Chen, Á. González-Vila, F. Liu, Y. Liu, K. Li, T. Guo, Twist sensor based on surface plasmon resonance excitation using two spectral combs in one tilted fiber Bragg grating, *J. Opt. Soc. Am. B* 36 (5) (2019) 1176–1182.
- [25] B. Han, Y.-N. Zhang, X. Wang, D. Yang, Y. Liu, J. Sun, Y. Wang, High-sensitive fiber anemometer based on surface plasmon resonance effect in photonic crystal fiber, *IEEE Sens. J.* 19 (9) (2019) 3391–3398.
- [26] J. García, D. Monzón-Hernández, J. Manríquez, E. Bustos, One step method to attach gold nanoparticles onto the surface of an optical fiber used for refractive index sensing, *Opt. Mater.* 51 (2016) 208–212.
- [27] J. Cao, E. Galbraith, T. Sun, K. Grattan, Comparison of surface plasmon resonance and localized surface plasmon resonance-based optical fibre sensors, *J. Phys. Conf. Ser.* 307 (1) (2011) 012050.
- [28] V. Amendola, R. Pilot, M. Frascioni, O.M. Marago, M.A. Iatì, Surface plasmon resonance in gold nanoparticles: a review, *J. Phys. -Condens. Mat.* 29 (20) (2017) 203002.
- [29] X. Qian, H.S. Park, The influence of mechanical strain on the optical properties of spherical gold nanoparticles, *J. Mech. Phys. Solids* 58 (3) (2010) 330–345.
- [30] W. Cai, H. Hofmeister, M. Dubiel, Importance of lattice contraction in surface plasmon resonance shift for free and embedded silver particles, *Eur. Phys. J. D* 13 (2) (2001) 245–253.
- [31] J. Lerme, M. Pellarin, E. Cottancin, M. Gaudry, M. Broyer, N. Del Fatti, F. Vallee, C. Voisin, Influence of lattice contraction on the optical properties and the electron dynamics in silver clusters, *Eur. Phys. J. D* 17 (2) (2001) 213–220.
- [32] W. Somerville, B. Auguié, E. Le Ru, Accurate and convergent T-matrix calculations of light scattering by spheroids, *J. Quant. Spectrosc. Ra.* 160 (2015) 29–35.
- [33] W. Somerville, B. Auguié, E. Le Ru, Smarties: User-friendly codes for fast and accurate calculations of light scattering by spheroids, *J. Quant. Spectrosc. Ra.* 174 (2016) 39–55.
- [34] S.I. Ranganathan, M. Ostoj-Starzewski, Universal elastic anisotropy index, *Phys. Rev. Lett.* 101 (5) (2008) 055504.
- [35] J. Cao, T. Sun, K.T. Grattan, Gold nanorod-based localized surface plasmon resonance biosensors: a review, *Sensor. Actuat. B-Chem.* 195 (2014) 332–351.
- [36] C.F. Bohren, D.R. Huffman, Absorption and scattering of light by small particles, John Wiley & Sons, 1998.
- [37] G.N. Greaves, A. Greer, R.S. Lakes, T. Rouxel, Poisson's ratio and modern materials, *Nat. Mater.* 10 (11) (2011) 823–837.
- [38] L.B. Scaffardi, J.O. Tocho, Size dependence of refractive index of gold nanoparticles, *Nanotechnology* 17 (5) (2006) 1309–1315.
- [39] P.B. Johnson, R.-W. Christy, Optical constants of the noble metals, *Phys. Rev. B* 6 (12) (1972) 4370.
- [40] A.D. Rakić, A.B. Djurišić, J.M. Elazar, M.L. Majewski, Optical properties of metallic films for vertical-cavity optoelectronic devices, *Appl. Opt.* 37 (22) (1998) 5271–5283.
- [41] M.I. Mishchenko, L.D. Travis, A.A. Lacis, Scattering, absorption, and emission of light by small particles, Cambridge Univ. Press, 2002.
- [42] W. Somerville, B. Auguié, E. Le Ru, A new numerically stable implementation of the T-matrix method for electromagnetic scattering by spheroidal particles, *J. Quant. Spectrosc. Ra.* 123 (2013) 153–168.
- [43] W.R. Somerville, B. Auguié, E.C. Le Ru, Simplified expressions of the T-matrix integrals for electromagnetic scattering, *Opt. Lett.* 36 (17) (2011) 3482–3484.
- [44] F. Xu, A.B. Davis, Derivatives of light scattering properties of a nonspherical particle computed with the T-matrix method, *Opt. Lett.* 36 (22) (2011) 4464–4466.
- [45] W.B. Hillig, Strength of bulk fused quartz, *J. Appl. Phys.* 32 (4) (1961), 741–741.
- [46] Y. Hua, L. Gu, H. Watanabe, Micromechanical analysis of nanoparticle-reinforced dental composites, *Int. J. Eng. Sci.* 69 (2013) 69–76.
- [47] S. Kim, D.C. Ratchford, X. Li, Atomic force microscope nanomanipulation with simultaneous visual guidance, *ACS Nano* 3 (10) (2009) 2989–2994.
- [48] H. McSkimin, Measurement of elastic constants at low temperatures by means of ultrasonic waves—data for silicon and germanium single crystals, and for fused silica, *J. Appl. Phys.* 24 (8) (1953) 988–997.
- [49] P. Vlугter, Y. Bellouard, Elastic properties of self-organized nanogratings produced by femtosecond laser exposure of fused silica, *Phys. Rev. Mater.* 4 (2) (2020) 023607.
- [50] C.D. Butter, G. Hocker, Fiber optics strain gauge, *Appl. Optics* 17 (18) (1978) 2867–2869.
- [51] A. Bertholds, R. Dandliker, Determination of the individual strain-optic coefficients in single-mode optical fibres, *J. Lightwave Technol.* 6 (1) (1988) 17–20.